

Molecular screening in nuclear reactions

A. Cvetinovic, M. Lipoglavsek, S. Markelj, and J. Vesic
Jozef Stefan Institute, Ljubljana, Slovenia

(Received 24 June 2015; revised manuscript received 8 October 2015; published 7 December 2015)

The dependence of electron screening in nuclear reactions on projectile or target atomic number has been studied by bombarding different hydrogen-containing targets with beams of ${}^7\text{Li}$, ${}^{11}\text{B}$, and ${}^{19}\text{F}$. The largest electron screening potentials were obtained in a graphite target containing hydrogen as an impurity. Some measured potentials are almost two orders of magnitude above the theoretical predictions. To explain the measurements, a new concept of electron screening is introduced.

DOI: [10.1103/PhysRevC.92.065801](https://doi.org/10.1103/PhysRevC.92.065801)

PACS number(s): 25.40.Lw, 25.40.Ny, 25.90.+k

I. INTRODUCTION

Electron screening is omnipresent in nuclear reactions induced by charged particles. It is thought that it can be neglected at energies much above atomic binding energies, based on a rather simple theory [1] placing electrons at the atomic radius and assuming a constant potential inside a uniformly charged spherical atomic shell. We will show that a different type of electron screening exists in proton capture reactions.

Electron screening is nevertheless important in nuclear astrophysics. This can be seen in two ways. For nucleosynthesis calculations precise reaction rates should be known at very low energies. At these energies the charged-particle-induced reaction cross sections become increasingly more difficult to measure due to their sharp decrease with decreasing energy. The energies of astrophysical interest can only be reached in exceptional circumstances, such as in the measurements in underground laboratories [2]. However, even when astrophysical energies are actually reached, the measurements do not give the nuclear cross section. Since in the laboratory the nuclei are always surrounded by atomic electrons, the measured cross sections are enhanced by electron screening. To get to the bare nuclear cross section, the electron screening effect has to be decoupled from the measurement, which is not as easy as might be inferred from Ref. [1]. One way to circumvent this problem is to measure the cross section indirectly, such as with the Trojan Horse method [3], but this method can only be applied to a limited number of reactions.

The importance of electron screening can also be viewed from the opposite point. Namely, almost all reactions in stars occur at low energies where electron screening cannot be neglected. It is believed that electron screening in stellar plasmas differs from the laboratory screening. A classical theory [4] on electron dynamics together with the simple view of Ref. [1] were employed to describe electron screening in plasma. Unfortunately, there is at present no way to check whether such extremely simplified assumptions are actually valid. One thing that can be performed is to try to understand the laboratory screening better and to draw parallels between laboratory and plasma. The present paper aims at that.

When studying nuclear reactions at low energies, one usually transforms the cross section σ into the astrophysical $S(E)$ factor with the relation,

$$\sigma(E) = \frac{S(E)}{E} e^{-2\pi\eta}, \quad (1)$$

where E is the center-of-mass energy and η is the Sommerfeld parameter $\eta = Z_1 Z_2 e^2 / (4\pi \epsilon_0 \hbar c) (\mu c^2 / 2E)^{1/2}$. Here Z_1 and Z_2 are the charge numbers of the interacting nuclei, and μ is their reduced mass. At low energies the cross sections are enhanced by an enhancement factor f that takes into account different barrier penetrabilities through screened (σ_s) and bare (σ_b) Coulomb barriers [1,5],

$$f(E) = \frac{\sigma_s}{\sigma_b} = \frac{e^{-2\pi\eta(E+U_e)}}{e^{-2\pi\eta(E)}}, \quad (2)$$

where U_e is the electron screening potential defined as [1] $U_e = Z_1 Z_2 e^2 / 4\pi \epsilon_0 R_a$. Setting R_a equal to the radius of the innermost electrons of the target (or projectile) atoms, i.e., $R_a = R_B / Z_1$ with the Bohr radius R_B , the resulting U_e equals the adiabatic potential U_{ad} . For the reactions studied in our paper, U_{ad} 's are listed in Table I. It should be pointed out that these U_{ad} 's are the maximum values allowed by the theory [1]. However, many publications from different groups quote measured U_e values way above the theoretically predicted ones [3,5–12]. Most publications deal with the screening potential in the ${}^2\text{H}(d,p){}^3\text{H}$ reaction. In all of these cases deuterium was implanted into various materials, and very different U_e values were obtained from different implanted targets. The reason for this variability has not been firmly established yet. Raiola *et al.* [7] restricted the large electron screening effect to metallic host materials, whereas their measurements in insulating and gaseous targets were consistent with the adiabatic limit [1]. Kasagi [8], on the other hand, observed the largest electron screening in a PdO insulator. Cruz *et al.* [9] extended these measurements to the ${}^7\text{Li}(p,\alpha){}^4\text{He}$ reaction where lithium was implanted into a palladium host material and a linear dependence of U_e on the target Z number was suggested. Our group studied the same reaction in inverse kinematics and a dependence of U_e on the target preparation was observed [11,12].

II. EXPERIMENT

In the present paper, we studied the dependence of the electron screening potential on the atomic number Z by measuring the reaction rates of the ${}^1\text{H}({}^7\text{Li},\alpha){}^4\text{He}$, ${}^1\text{H}({}^{11}\text{B},\alpha\alpha){}^4\text{He}$, and ${}^1\text{H}({}^{19}\text{F},\alpha\gamma){}^{16}\text{O}$ reactions. All reactions were studied in inverse kinematics on physically the same targets. This has never been tried before, and it gave us a unique opportunity to look at the Z dependence of U_e . We used five different targets

TABLE I. Electron screening potentials for different nuclear reactions and targets together with target hydrogen bulk stoichiometry. The calculation of the adiabatic limit U_{ad} [1] is also presented.

Target	Stoichio-metry	U_e (keV)		
		${}^7\text{Li}$	${}^{11}\text{B}$	${}^{19}\text{F}$
U_{ad}		0.24	0.68	2.19
TiH	1.03 ± 0.04	3.9 ± 0.4	6.7 ± 1.8	62 ± 6
Pd	0.21 ± 0.03	3.6 ± 0.7	8.0 ± 1.9	63 ± 6
W	$(4.2 \pm 0.2)10^{-2}$	5.9 ± 0.9		74 ± 15
Graphite	$(5.9 \pm 0.3) 10^{-2}$	10.3 ± 0.4	32 ± 4	115 ± 8

containing hydrogen. Each target was prepared in a different way. For a standard hydrogen target we used polyimide (Kapton, $\text{C}_{22}\text{H}_{10}\text{N}_2\text{O}_5$) due to its relative insensitivity to radiation damage. The second target was titanium hydride pressed from TiH powder into a 1-mm-deep hole in a Cu backing which helped to cool the target after heating with the beam. The third sample was a 250- μm -thick graphite foil obtained from Chempur. It contained already about 6 at. % of hydrogen as received, and we implanted additional hydrogen with our ion gun at an energy of 5 keV. The fourth target was a 250- μm -thick palladium foil, first loaded and unloaded with hydrogen several times. The cycling was performed by leaving the Pd foil in hydrogen gas at 1 bar for 24 h and then heating in vacuum to 300 °C. After that the Pd foil was radiation damaged by 45.3×10^{15} ${}^{19}\text{F}$ ions per cm^2 at 7.8 MeV and again left in hydrogen gas at 1 bar for a few hours. The final target was a tungsten sample, produced by Plansee, that was mechanically polished and outgassed at 1200 K for stress relief. Electron microscopy showed large grains (5–20 μm) [13]. It was first irradiated with 20-MeV ${}^{186}\text{W}$ ions creating radiation damage with maximum 0.45 displacements per atom to a depth of 2.5 μm . The sample was implanted with 5-keV hydrogen ions from the ion gun with a beam intensity of 0.8 mA/ cm^2 in $\frac{1}{2}$ -h steps. The maximum hydrogen concentration was achieved already after the first $\frac{1}{2}$ h, thus saturating the damaged zone with hydrogen. The ${}^7\text{Li}$, ${}^{11}\text{B}$, and ${}^{19}\text{F}$ beams were provided by the 2 MV Tandatron accelerator at Jozef Stefan Institute. The outgoing α particles were measured by a silicon detector placed 2.9 cm from the target at an angle of 135° with respect to the beam direction. The 6129-keV ${}^{16}\text{O}$ γ ray was measured by a germanium detector placed 4.2 cm from the target at an angle of 135°. The beam dose was deduced from the measurement of electric charge deposited inside an electrically insulated target chamber. The charge was also collected from the absorber in front of the silicon detector, so the only hole through which we could lose some charge was the beam entrance to the chamber. However, the area of this hole represented less than 0.1% of 4π , and we are confident that we measured almost the whole charge entering the target chamber including the scattered δ electrons. Since the beam currents were on the order of 1 μA and no measurement lasted less than a few minutes, the charge measurement was very accurate.

During the experiment the hydrogen concentration in the sample was controlled by repeatedly measuring at the same beam energy after each measurement at a different energy. The

Pd and TiH targets did not show any loss of hydrogen during any of our experiments. The W target lost some hydrogen only during bombardment with ${}^{19}\text{F}$ ions, and this was corrected by normalizing the γ -ray yields to control measurements before and after the measurement. Both Kapton and graphite targets showed loss of hydrogen during all experiments, and the yields were normalized to control measurements. The Kapton target was moved to a different spot when the reaction yield in the control measurement decreased by more than 35% of the original one. All targets represented thick hydrogen targets. The Kapton, graphite, Pd, and TiH targets had uniform hydrogen distribution, whereas the W target exhibited a surface hydrogen peak and a uniform distribution in the bulk (see below).

III. RESULTS

First we analyzed the data in the same way as was performed in most of the previous experiments [1,7,9,12]. The ${}^1\text{H}({}^7\text{Li}, \alpha){}^4\text{He}$ reaction does not have any known resonances in the lithium energy range between 0.4 and 2 MeV. Therefore, the α -particle yields were obtained by integrating the cross section as a function of energy. The $S(E)$ factor was taken from Ref. [3], and the α -particle angular distribution was taken from Ref. [14]. Electron screening was taken into account according to Eq. (2), and U_e and hydrogen stoichiometry (calculated as the number of H atoms per target atom other than H) were free parameters in the fit. The integrated enhancement factors for the ${}^7\text{Li}$ reaction in different targets are shown in Fig. 1, and the obtained U_e and hydrogen stoichiometry are listed in Table I.

In the ${}^1\text{H}({}^{11}\text{B}, \alpha\alpha){}^4\text{He}$ and ${}^1\text{H}({}^{19}\text{F}, \alpha\gamma){}^{16}\text{O}$ reactions we measured the resonances at $E_r = 149$ and 323 keV in the center-of-mass system, respectively. The resonance strengths $\omega\gamma$ were obtained from the measured yields Y from the equation [15],

$$Y = \frac{\lambda^2 \omega\gamma}{2\pi \varepsilon_r} \left[\arctan \left(\frac{E - E_r}{\Gamma/2} \right) + \frac{\pi}{2} \right], \quad (3)$$

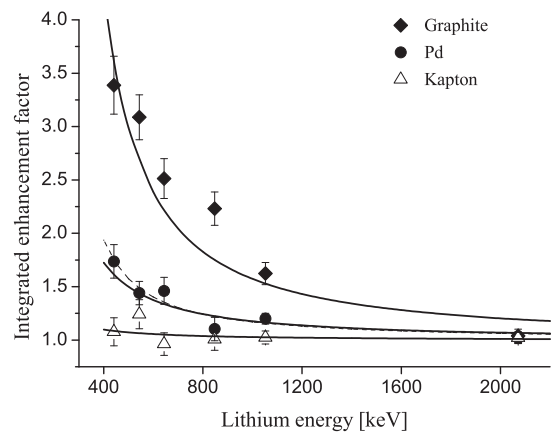


FIG. 1. Integrated enhancement factors f as a function of lithium beam energy for the ${}^1\text{H}({}^7\text{Li}, \alpha){}^4\text{He}$ reaction in graphite, Pd, and Kapton targets. The solid lines represent calculations with the integrated version of Eq. (2), whereas the dashed line comes from the integral of Eq. (4). See Ref. [12] for the functional form of the integrals.

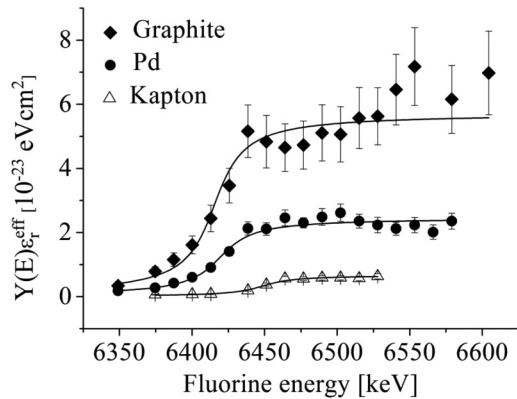


FIG. 2. γ -ray yields for the $^1\text{H}(^{19}\text{F}, \alpha\gamma)^{16}\text{O}$ reaction multiplied by the effective stopping power as a function of fluorine beam energy for graphite, Pd, and Kapton targets near the resonance energy of 323 keV in the center-of-mass (or 6.47 MeV in the laboratory) system. The solid lines represent fits with Eq. (3).

where λ is the de Broglie wavelength of the beam, ϵ_r is its effective stopping power in the target calculated with the SRIM code [16], and Γ is the resonance width. For all five targets the hydrogen stoichiometry in ^{11}B and ^{19}F experiments was taken from the lithium experiment since the experiments were performed immediately after each other. Only $\omega\gamma$, Γ , and E_r were fitted. The electron screening was again taken into account according to Eq. (2) since $\omega\gamma$ is proportional to σ , and the fitted $\omega\gamma$ for Kapton was taken as the bare resonance strength. The surface peak in the W target did not result from surface contamination but from a larger number of hydrogen trapping sites at the surface [17]. Therefore, the W target was treated as a sum of a thin and a thick target, and we assumed that the U_e on the surface equals the one in the bulk. The calculated and measured yields Y for the ^{19}F reaction are shown in Fig. 2 as a function of beam energy around the resonance energy of 6.47 MeV in the laboratory system. The measured yields depend on the resonance energy, probing the surface concentration at the resonance energy whereas at higher energies the concentration below the surface is probed due to the ion stopping in the target. One can observe that above the resonance energy the measured yields are constant indicating a constant hydrogen distribution throughout the analyzing depth. The results for U_e from all reactions are listed in Table I.

Since the results critically depend on the stopping powers, we are listing some of the used ones in Table II. As expected, they do not vary significantly from one target to another. We checked all calculated stopping powers with experimental results. For the ^7Li beam, measurements exist for all targets except Kapton and the agreement with calculations is always good [16]. The various stopping power measurements for lithium in carbon and titanium cover a range of energies from about 0.6 MeV down to below 1 keV. The measurements in palladium cover a narrower range between about 100 and 20 keV. For the tungsten target only two measurements exist at 0.5 MeV, however, the neighboring tantalum is well covered with measurements between 300 and 2 keV. Only one stopping power measurement exists for both boron and fluorine ions in the carbon target, but the neighboring carbon

TABLE II. Stopping powers $dE/dx\rho$ calculated with the SRIM code [16]. For the ^7Li beam they are given at 400 keV and for the ^{11}B and ^{19}F beams at the resonance energies of 1.79 and 6.47 MeV, respectively.

Target	Stopping power (MeV cm ² /mg)		
	^7Li	^{11}B	^{19}F
Graphite	2.36	5.68	12.2
TiH	1.38	3.70	8.57
Pd	0.58	1.79	4.38
W	0.36	1.11	2.78
Kapton	2.15	5.39	12.2

and oxygen ion stopping power measurements cover the energies of interest for our experiment. There is a similar situation in the titanium target, which has more fluorine measurements, but the oxygen measurements were performed at energies of our interest. No measurements exist for boron or fluorine in palladium, but the neighboring silver is well covered. Similarly, oxygen ion stopping power measurements were performed in tantalum at the energies of our fluorine beam. The prescribed compound correction of -7.2% for Kapton was taken into account for all beams. The differences between the measured and the calculated stopping powers are never much larger than 10%, so the use of wrong stopping powers clearly cannot explain the large enhancement factors observed in our experiment. Similarly, our results also strongly depend on our assumption of a uniform hydrogen distribution inside the targets. We checked the hydrogen distribution with the elastic recoil detection analysis (ERDA) method where elastically scattered protons were detected at an angle of 45° with respect to the direction of a 4.3-MeV ^7Li beam. The cross section from Ref. [18] was used for the analysis of the ERDA measurements with the SIMNRA code [19]. The ERDA measurements also showed a uniform hydrogen distribution in all targets except tungsten down to a depth of about 0.5 μm (in graphite). Uniform distributions to a depth of about 0.3 μm can also be seen in Fig. 2. We could determine hydrogen concentrations from the ERDA measurements, and the results agreed with the stoichiometry deduced from the lithium measurements. However, the uncertainties of the concentrations deduced from the ERDA measurements were larger than the ones deduced from the lithium measurements, and therefore, we used the later ones in our analysis. The only exception to this rule was the Pd target for which we could gravimetrically determine the hydrogen concentration more precisely by subtracting the weight of the empty foil from the weight of the filled one. Also this measurement agreed very well with the other measurements of concentration, but for the sake of consistency, we used the stoichiometry deduced from the lithium measurement for the Pd target as well. Another result came out of the ERDA measurements. Like many other polymers, Kapton also is hygroscopic. We observed that our foil contained about two water molecules per Kapton molecule, resulting in hydrogen stoichiometry of 13.4(1) instead of 10.

Surprisingly, the largest electron screening was found for all three reactions in the graphite target, followed by the W, Pd, TiH, and Kapton targets. For the lithium reaction in

Kapton the U_e was consistent with 0 within the error bar. We were especially cautious about the interpretation of the surprising results in the graphite target. To eliminate a possible misinterpretation we repeated all measurements with three different graphite targets, and one of them was also turned by 180° , and the measurements were repeated on its back side. All four measurements agreed with each other, which eliminates a possible misinterpretation due to the orientation of the graphite target. Fortunately, the α -particle angular distributions below 1 MeV are mostly isotropic in the lithium reaction [14], and after emitting an α particle in the fluorine reaction the excited ^{16}O nucleus does not retain a preferential orientation. The γ rays emitted from a nucleus at rest are again emitted isotropically [20]. The observed results therefore cannot be due to different angular distributions in different targets. However, the most compelling evidence of the last statement came from the Pd target. We used the same Pd target before and after it was radiation damaged. Without radiation damage this target showed no evidence of a large electron screening effect in the lithium reaction [11], but after damaging the target with fluorine ions, the large electron screening occurred. This also proves that the results could not be due to different equilibrium charge states of the projectiles in different targets.

IV. DISCUSSION

We interpret the measurements in the following way. The presence of a hydrogen impurity atom in the hexagonal graphite lattice forces the nearest carbon atom out of the sheet plane [21], thus creating a lattice distortion. This places the proton always closer to one carbon atom than to the others and puts it in the path of the lattice atomic electrons that can come close to it. The tungsten lattice on the other hand was radiation damaged, and protons got trapped in crystal lattice vacancies and dislocations [22] where they are again closer to one W atom than to the others. The reason why U_e is lower in W than in graphite is that in polycrystalline metals, hydrogen can also get trapped at grain boundaries and voids [22] where we assume the electron screening is low. This means the effective electron screening for the two separate trapping sites is lower. The Pd crystal lattice was also radiation damaged, but it was not annealed contrary to W, which means it had smaller grains with more grain boundaries, and the resulting effective U_e is lower than in W. The TiH target did not have the full TiH_2 stoichiometry since the powder had been stored in air for several years. At the measured stoichiometry of 1.03, $\text{TiH}_{1.03}$ is a mixture of fcc and tetragonal fct lattices [23]. The presence of the tetragonal distortions in our target was confirmed by x-ray diffraction measurements, which showed similar spectra as after heat treatment in Ref. [24]. As we have shown in the case of Pd [11], the hydrogen on regular interstitial sites in the fcc lattice did not produce a large electron screening effect. Only when the protons are pulled away from their fcc equilibrium positions does a large screening effect occur. This is the case in the fct lattice in TiH. The above considerations result in a modified enhancement factor,

$$f_{\text{mod}} = (1 - C) \frac{e^{-2\pi\eta(E+U_{\text{ad}})}}{e^{-2\pi\eta(E)}} + C \frac{e^{-2\pi\eta(E+U_e)}}{e^{-2\pi\eta(E)}}, \quad (4)$$

TABLE III. Enhancement factors for the boron and fluorine reactions from experiment and calculation with Eq. (4). The fraction of protons on dislocated sites C is listed.

Target	C	Enhancement factor f_{mod}			
		^{11}B expt.	^{11}B calc.	^{19}F expt.	^{19}F calc.
TiH	0.28 ± 0.02	1.3 ± 0.1	1.6 ± 0.1	3.6 ± 0.4	3.1 ± 0.4
Pd	0.28 ± 0.04	1.4 ± 0.1	1.6 ± 0.1	3.7 ± 0.4	3.1 ± 0.4
W	0.51 ± 0.05		2.1 ± 0.2	4.5 ± 1.5	4.9 ± 0.6

where U_{ad} is the small electron screening potential from the adiabatic limit, U_e is the large potential from the graphite target, and the factor C is the fraction of hydrogen on dislocated lattice sites. The values of C were determined from the lithium reaction assuming that in graphite all hydrogen is on dislocated sites. The f_{mod} 's were calculated for the boron and fluorine induced reactions for W, Pd, and TiH targets, whereas for graphite the calculation by definition equals the experiment. The results are listed in Table III, and the agreement with the measured enhancement factor is good, taking into account that the dependence on U_e is exponential.

However, the very large electron screening potentials in the graphite target for different projectiles still need to be explained. The measured values are about a factor of 50 above the adiabatic limit prediction and much higher than any potential measured so far. The Z dependence seems to be higher than quadratic. This rules out any theory based on static electron densities and renders the above analysis based on U_e obsolete. Instead, we propose a process we call molecular screening. In the H_2^+ molecular ion the electron resides between the two protons most of the time. Similarly, during the reaction process, an electron of the lattice atom may be caught in the attractive potential of the two approaching nuclei. Normally, when the two nuclei are close enough, the electron would behave as an atomic electron of a nucleus with $Z = Z_1 + Z_2$, resulting in U_{ad} . The character of the electron wave function changes from bonding (between the two nuclei) to nonbonding (single electron ion) when its binding energy exceeds the ionic binding energy. In the hydrogen molecular ion this happens just below $0.1 R_B$ [25]. However, there is a certain probability that the electron stays between the two nuclei all the time until the reaction actually occurs. In case one of the reactants is a proton, the reaction proceeds similarly to neutron capture since the proton charge is completely screened. In such a case, there is no Coulomb barrier to the reaction. The probability is related to the time it takes from the capture of the electron to the nuclear reaction. All measurements so far show an exponential-like increase in the enhancement factor with decreasing energy. Therefore, to explain the measurements, the probability needs to depend exponentially on time by analogy to the exponential decay of an excited state. Taking into account two different reaction paths, we can define an enhancement factor similar to Eq. (4) but with the parameter K denoting the fraction of electrons remaining between the two reactants until the time of the reaction,

$$f_1 = (1 - K) \frac{e^{-2\pi\eta(E+U_{\text{ad}})}}{e^{-2\pi\eta(E)}} + K e^{2\pi\eta(E)-t/\tau}, \quad (5)$$

TABLE IV. Enhancement factors for the boron and fluorine reactions from experiment and calculation with Eq. (5). The fraction of protons remaining between the reactants K is listed.

Target	K	Enhancement factor f_1			
		^{11}B expt.	^{11}B calc.	^{19}F expt.	^{19}F calc.
Graphite	$(1.0 \pm 0.1)10^{-2}$	3.1 ± 0.4	3.1 ± 0.3	8.7 ± 1.0	9.3 ± 0.9

where $t = \frac{R_B}{Z} \sqrt{\frac{\mu}{2E}}$ denotes the time since the proton passed beyond the innermost projectile electron. We have fitted Eq. (5) to our lithium data in graphite shown in Fig. 1 with two free parameters K and τ . The fit indicates that $K = 0.010(1)$ and that the lifetime τ of such a state should be $7.6(1) \times 10^{-18}$ s. Assuming that τ is inversely proportional to Z^2 , we get for enhancement factors in beryllium and fluorine reactions the results listed in Table IV. The agreement between experiment and calculation is surprisingly good.

Incidentally, the scaling of our graphite measurements agrees with the highest measured screening potential of 0.8 keV in the $^2\text{H}(d, p)^3\text{H}$ reaction [7], and our Eq. (4) could also be used to explain the very different electron screening potentials reported for different targets in Refs. [7,8].

V. CONCLUSIONS

We have revealed a new aspect of the electron screening effect in nuclear reactions, which in certain conditions assumes a completely different form than previously thought. It is not yet clear what these conditions are and whether anywhere in the universe such conditions might exist during the nucleosynthesis or energy generation processes.

The final point we want to make is that any experiment studying proton capture in inverse kinematics, either a measurement of hydrogen concentration with nuclear reaction analysis [26] or a cross-section measurement with radioactive beams (see, e.g., Ref. [27]), should take into account large electron screening. Special care should be put into target preparation since the position of hydrogen in the target is relevant for the measured reaction rate.

ACKNOWLEDGMENTS

The authors are grateful to Dr. O. V. Ogorodnikova from the Max Planck Institute für Plasmaphysik for providing the tungsten sample irradiated with W ions. We would also like to thank S. Skapin from the Jozef Stefan Institute for performing the x-ray diffraction measurements of the TiH samples.

-
- [1] H. J. Assenbaum, K. Langanke, and C. Rolfs, *Z. Phys. A: At. Nucl.* **327**, 461 (1987).
- [2] C. Broggini *et al.*, *Ann. Rev. Nucl. Part. Sci.* **60**, 53 (2010).
- [3] L. Lamia *et al.*, *Astron. Astrophys.* **541**, A158 (2012).
- [4] C. Rolfs and W.S. Rodney, *Cauldrons in the Cosmos* (University of Chicago Press, Chicago, 1988).
- [5] A. Huke, K. Czerski, P. Heide, G. Ruprecht, N. Targosz, and W. Żebrowski, *Phys. Rev. C* **78**, 015803 (2008).
- [6] K. Czerski *et al.*, *J. Phys. G: Nucl. Part. Phys.* **35**, 014012 (2008).
- [7] F. Raiola *et al.*, *Eur. Phys. J. A* **19**, 283 (2004).
- [8] J. Kasagi, *Prog. Theor. Phys. Suppl.* **154**, 365 (2004).
- [9] J. Cruz *et al.*, *Phys. Lett. B* **624**, 181 (2005).
- [10] F. Raiola *et al.*, *J. Phys. G: Nucl. Part. Phys.* **31**, 1141 (2005).
- [11] M. Lipoglavsek *et al.*, *Eur. Phys. J. A* **44**, 71 (2010).
- [12] J. Vesic *et al.*, *Eur. Phys. J. A* **50**, 153 (2014).
- [13] O. Ogorodnikova *et al.*, *J. Nucl. Mater.* **451**, 379 (2014).
- [14] S. Engstler *et al.*, *Z. Phys. A: Hadrons Nucl.* **342**, 471 (1992).
- [15] C. Iliadis, *Nuclear Physics of Stars* (Wiley, Hoboken, NJ, 2008), p. 341.
- [16] J. F. Ziegler *et al.*, *The Stopping and Range of Ions in Matter* (Lulu, Morrisville, NC, 2008); www.srim.org.
- [17] S. Markelj *et al.*, *Appl. Surf. Sci.* **282**, 478 (2013).
- [18] Z. Siketic *et al.*, *Nucl. Instrum. Methods Phys. Res., Sect. B* **229**, 180 (2005).
- [19] M. Mayer, in *SIMNRA, A Simulation Program for the Analysis of NRA, RBS, and ERDA*, edited by J. L. Duggan, B. Stippec, and I. L. Morgan, AIP Conf. Proc. No. 475 (AIP, New York, 1999), p. 541; home.rzg.mpg.de/~mam/.
- [20] S. Croft, *Nucl. Instrum. Methods Phys. Res., Sect. A* **307**, 353 (1991).
- [21] C. Herrero and R. Ramirez, *J. Phys. D: Appl. Phys.* **43**, 255402 (2010).
- [22] Y. Fukai, *The Metal Hydrogen System* (Springer, Berlin, 2005), Chap. 5.
- [23] C. P. Liang and H. R. Gong, *Mater. Lett.* **115**, 252 (2014).
- [24] D. Mandrino *et al.*, *Mater. Charact.* **72**, 87 (2012).
- [25] H. Wind, *J. Chem. Phys.* **42**, 2371 (1965).
- [26] M. Mayer *et al.*, *Nucl. Instrum. Methods Phys. Res., Sect. B* **267**, 506 (2009).
- [27] S. D. Pain *et al.*, *Phys. Rev. Lett.* **114**, 212501 (2015).